28

Modeling and Numerical Simulation of Ferroelectric Material Behavior Using Hysteresis Operators

Manfred Kaltenbacher and Barbara Kaltenbacher
Alps-Adriatic University Klagenfurt
Austria

1. Introduction

The piezoelectric effect is a coupling between electrical and mechanical fields within certain materials that has numerous applications ranging from ultrasound generation in medical imaging and therapy via acceleration sensors and injection valves in automotive industry to high precision positioning systems. Driven by the increasing demand for devices operating at high field intensities especially in actuator applications, the field of hysteresis modeling for piezoelectric materials is currently one of highly active research. The approaches that have been considered so far can be divided into four categories:

(1) *Thermodynamically consistent models* being based on a macroscopic view to describe microscopical phenomena in such a way that the second law of thermodynamics is satisfied, see e.g., Bassiouny & Ghaleb (1989); Kamlah & Böhle (2001); Landis (2004); Linnemann et al. (2009); Schröder & Romanowski (2005); Su & Landis (2007).

(2) *Micromechanical models* that consider the material on the level of single grains, see, e.g., Belov & Kreher (2006); Delibas et al. (2005); Fröhlich (2001); Huber (2006); Huber & Fleck (2001); McMeeking et al. (2007).

(3) *Phase field models* that describe the transition between phases (corresponding to the motion of walls between domains with different polarization orientation) using the Ginzburg Landau equation for some order parameter, see e.g., Wang et al. (2010); Xu et al. (2010).

(4) *Phenomenological models using hysteresis operators* partly originating from the input-output description of piezoelectric devices for control purposes, see e.g., Ball et al. (2007); Cimaa et al. (2002); Hughes & Wen (1995); Kuhnen (2001); Pasco & Berry (2004); Smith et al. (2003).

Also multiscale coupling between macro- and microscopic as well as phase field models partly even down to atomistic simulations have been investigated, see e.g., Schröder & Keip (2010); Zäh et al. (2010).

Whereas most of the so far existing models are designed for the simulation of polarization, depolarization or cycling along the main hysteresis loop, the simulation of actuators requires the accurate simulation of *minor loops* as well.

Moreover, the physical behavior can so far be reproduced only qualitatively, whereas the use of models in actuator simulation (possibly also aiming at simulation based optimization) needs to *fit measurements* precisely.
Simulation of a piezoelectric device with a possibly complex geometry requires not only an input-output model but needs to resolve the spatial distribution of the crucial electric and mechanical field quantities, which leads to partial differential equations (PDEs). Therewith, the question of *numerical efficiency* becomes important.
Preisach operators are phenomenological models for rate independent hysteresis that are capable of reproducing minor loops and can be very well fitted to measurements, see e.g., Brokate & Sprekels (1996); Krasnoselskii & Pokrovskii (1989); Krejčí (1996); Mayergoyz (1991); Visintin (1994). Moreover, they allow for a highly efficient evaluation by the application of certain memory deletion rules and the use of so-called Everett or shape functions.
In the following, we will first describe the piezoelectric material behavior both on a microscopic and macroscopic view. Then we will provide a discussion on the Preisach hysteresis operator, its properties and its fast evaluation followed by a description of our piezoelectric model for large signal excitation. In Sec. 4 we discuss the steps to incorporate this model into the system of partial differential equations, and in Sec. 5 the derivation of a quasi Newton method, in which the hysteresis operators are included into the system via incremental material tensors. For this set of partial differential equations we then derive the weak (variational) formulation and perform space and time discretization. The fitting of the model parameters based on relatively simple measurements is performed directly on the piezoelectric actuators in Section 6. The applicability of our developed numerical scheme will be demonstrated in Sec. 7, where we present a comparison of measured and simulated physical quantities. Finally, we summarize our contribution and provide an outlook on further improvements of our model to achieve a multi-axial ferroelectric and ferroelastic loading model.

2. Piezoelectric and ferroelectric material behavior

Piezoelectric materials can be subdivided into the following three categories

1. *Single crystals*, like quartz
2. *Piezoelectric ceramics* like barium titanate ($BaTiO_3$) or lead zirconate titanate (PZT)
3. *Polymers* like PVDF (polyvinylidenfluoride).

Since categories 1 and 3 typically show a weak piezoelectric effect, these materials are mainly used in sensor applications (e.g., force, torque or acceleration sensor). For piezoelectric ceramics the electromechanical coupling is large, thus making them attractive for actuator applications. These materials exhibit a polycrystalline structure and the key physical property of these materials is ferroelectricity. In order to provide some physical understanding of the piezoelectric effect, we will consider the microscopic structure of piezoceramics, partly following the exposition in Kamlah (2001).
A piezoelectric ceramic material is subdivided into grains consisting of unit cells with different orientation of the crystal lattice. The unit cells consist of positively and negatively charged ions, and their charge center position relative to each other is of major importance for the electromechanical properties. We will call the material *polarizable*, if an external load, e.g., an electric field can shift these centers with respect to each other. Let us consider $BaTiO_3$ or PZT, which have a polycrystalline structure with grains having different crystal lattice.

Above the Curie temperature T_c – for $BaTiO_3$ $T_c \approx 120\,^oC$ - $130\,^oC$ and for PZT $T_c \approx 250\,^oC$ - $350\,^oC$, these materials have the perovskite structure. The cube shape of a unit cell has a side length of a_0 and the centers of positive and negative charges coincide (see Fig. 1). However, below T_c the unit cell deforms to a tetragonal structure as displayed in Fig. 1, e.g.,

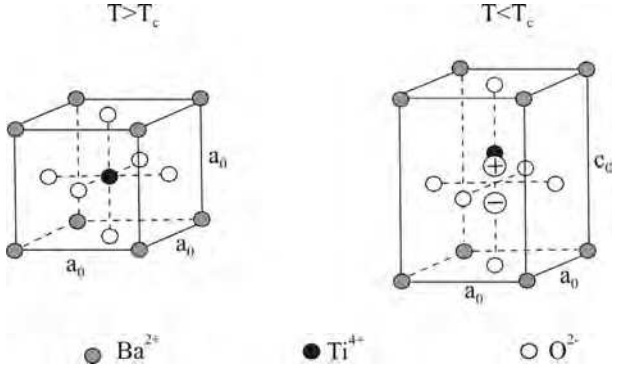

Fig. 1. Unit cell of $BaTiO_3$ above and below the Curie temperature T_c.

$BaTiO_3$ at room temperature changes its dimension by $(c_0 - a_0)/a_0 \approx 1\,\%$. In this ferroelectric

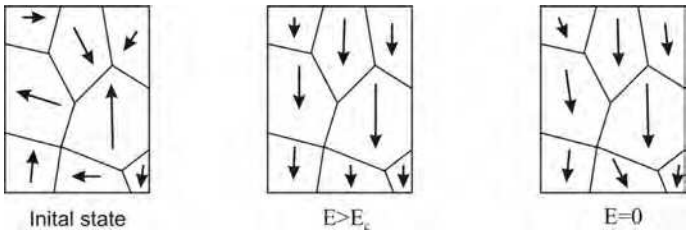

Fig. 2. Orientation of the polarization of the unit cells at initial state, due to a strong external electric field and after switching it off.

phase, the centers of positive and negative charges differ and a dipole is formed, hence the unit cell posses a spontaneous polarization. Since the single dipoles are randomly oriented, the overall polarization vanishes due to mutual cancellations and we call this the thermally depoled state or virgin state. This state can be modified by an electric or mechanical loading with significant amplitude. In practice, a strong electric field $E \approx 2\,\mathrm{kV/mm}$ will switch the unit cells such that the spontaneous polarization will be more or less oriented towards the direction of the externally applied electric field as displayed in Fig. 2. Now, when we switch off the external electric field the ceramic will still exhibit a non-vanishing residual polarization in the macroscopic mean (see Fig. 2). We call this the *irreversible* or *remanent polarization* and the just described process is termed as *poling*.

The *piezoelectric effect* can be easily understood on the unit cell level (see Fig. 1), where it just corresponds to an electrically or mechanically induced coupled elongation or contraction of both the c-axes and the dipole. Macroscopic piezoelectricity results from a superposition of this effect within the individual cells.

Ferroelectricity is not only relevant during the above mentioned poling process. To see this, let us consider a mechanically unclamped piezoceramic disc at virgin state and load the

electrodes by an increasing electric voltage. Initially, the orientation of the polarization within the unit cells is randomly distributed as shown in Fig. 3 (state 1). The switching of the domains

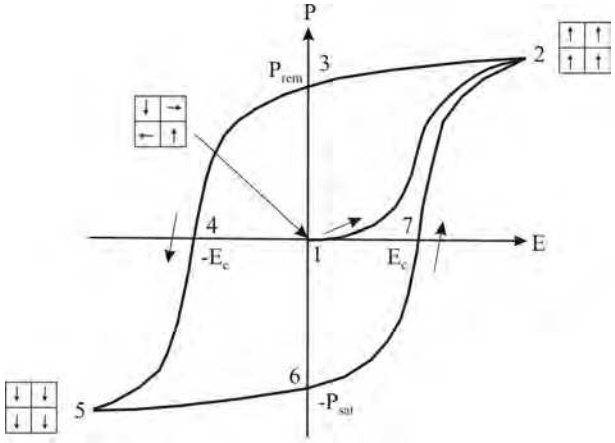

Fig. 3. Polarization P as a function of the electric field intensity E.

starts when the applied electric field reaches the so-called coercitive intensity E_c[1]. At this state, the increase of the polarization is much faster, until all domains are switched (see state 2 in Fig. 3). A further increase of the external electric loading would result in an increase of the polarization with only a relatively small slope and the occurring micromechanical process remains reversible. Reducing the applied voltage to zero will preserve the poled domain structure even at vanishing external electric field, and we call the resulting macroscopic polarization the remanent polarization P_{rem}. Loading the piezoceramic disc by a negative voltage of an amplitude larger than E_c will initiate the switching process again until we arrive at a random polarization of the domains (see state 4 in Fig. 3). A further increase will orient the domain polarization in the new direction of the external applied electric field (see state 5 in Fig. 3).

Measuring the mechanical strain during such a loading cycle as described above for the electric polarization, results in the so-called *butterfly curve* depicted in Fig. 4, which is basically a direct translation of the changes of dipoles (resulting in the total polarization shown in Fig. 3) to the c-axes on a unit cell level. Here we also observe that an applied electric field intensity $E > E_c$ is required in order to obtain a measurable mechanical strain. The observed strong increase between state 1 and 2 (or 7 and 2, respectively) is again a superposition of two effects: Firstly, we achieve an increase of the strain due to a reorientation of the c-axes into direction of the external electric field, which often takes place in two steps (90 degree and 180 degree switching). Secondly, the orientation of the domain polarization leads to the macroscopic piezoelectric effect yielding the reversible part of the strain. As soon as all domains are switched (see state 2 in Fig. 4), a further increase of the strain just results from the macroscopic piezoelectric effect. A separation of the switching (irreversible) and the piezoelectric (reversible) strain can best be seen by decreasing the external electric load to zero.

[1] It has to be noted that in literature E_c often denotes the electric field intensity at zero polarization. According to Kamlah & Böhle (2001) we define E_c as the electric field intensity at which domain switching occurs.

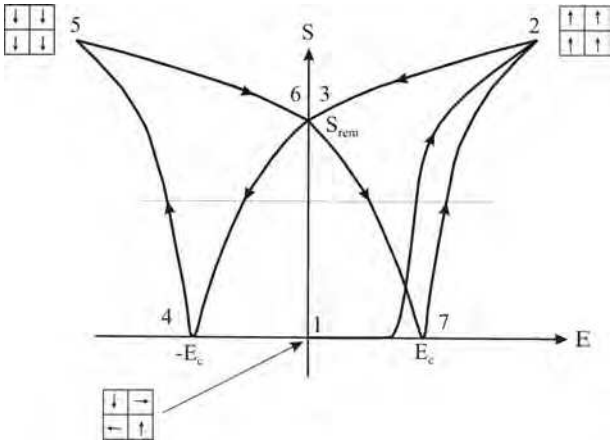

Fig. 4. Mechanical strain S as a function of the electric field intensity E.

Alternatively or additionally to this electric loading, one can perform a mechanical loading, which will also result in switching processes. For a detailed discussion on the occurring so-called ferroelastic effects we refer to Kamlah & Böhle (2001).

3. Preisach hysteresis operators

Hysteresis is a memory effect, which is characterized by a lag behind in time of some output in dependence of the input history. Figure 3, e.g., shows the curve describing the polarization P of some ferroelectric material in dependence of the applied electric field E: As E increases from zero to its maximal positive value E_{sat} at state 2 (virgin curve), the polarization also shows a growing behavior, that lags behind E, though. Then E decreases, and again P follows with some delay. As a consequence, there is a positive remanent polarization P_{rem} for vanishing E, that can only be completely removed by further decreasing E until a critical negative value is reached at state 4. After passing this threshold, a polarization in negative direction — so with the same orientation as E — is generated, until a minimal negative value is reached. The returning branch of the hysteresis curve ends at the same point $(E_{\text{sat}}, P_{\text{sat}})$ at state 2, where the outgoing branch had reversed but takes a different path, which results in a gap between these two branches and the typical closed main hysteresis loop. We write

$$P(t) = \mathcal{H}[E](t)$$

with some hysteresis operator $\mathcal{H}$. Normalizing input and output by their saturation values, e.g., $p(t) = P(t)/P_{\text{sat}}$ and $e(t) = E(t)/E_{\text{sat}}$, results in

$$p(t) = \mathcal{H}[e](t)\,.$$

In the remainder of this section we assume that both the input e and the output p are normalized so that their values lie within the interval $[-1, 1]$, and give a short overview on hysteresis operators following mainly the exposition in Brokate & Sprekels (1996) (see also Krejčí (1996) as well as Krasnoselskii & Pokrovskii (1989); Mayergoyz (1991); Visintin (1994)).

Probably the most simple example of hysteresis is the behavior of a switch or *relay* (see Fig. 5), that is characterized by two threshold values $\alpha > \beta$. The output value p is either -1 or $+1$ and changes only if the input value e crosses one of the switching thresholds α, β: If, at some time instance t, $e(t)$ increases from below to above α, the relay will switch up to $+1$, if e decreases from above to below β, it will switch down to -1, in all other cases it will keep its value — either plus or minus one, depending on the preceding history. Therefore, we just formally define the relay operator $\mathcal{R}_{\beta,\alpha}$ by

$$\mathcal{R}_{\beta,\alpha}[e] = p$$

according to the description above.

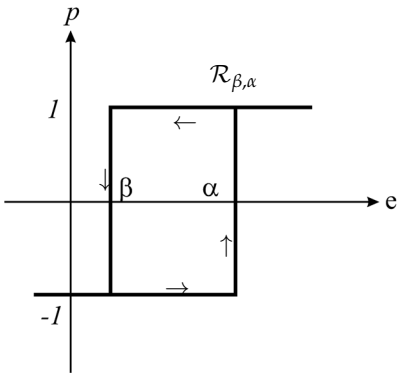

Fig. 5. Hysteresis of an elementary relay.

A practically important phenomenological hysteresis model that was originally introduced in the context of magnetism but plays a role also in many other hysteretic processes, is given by the *Preisach operator*

$$\mathcal{H}[e](t) = \iint_{\beta \le \alpha} \wp(\beta,\alpha)\mathcal{R}_{\beta,\alpha}[e](t)\, d(\alpha,\beta)\,, \tag{1}$$

which is a weighted superposition of elementary relays. The initial values of the relays $\mathcal{R}_{\beta,\alpha}$ (assigned to some "pre-initial" state e_{-1}) are set to

$$\mathcal{R}_{\beta,\alpha}[e_{-1}] = \begin{cases} -1 \text{ if } \alpha > -\beta \\ +1 \text{ else.} \end{cases} \tag{2}$$

Determining $\mathcal{H}$ obviously amounts to determining the weight function $\wp$ in Equation (1). The domain $\{(\beta,\alpha) \mid \beta \le \alpha\}$ of $\wp$ is called the *Preisach plane*. Assuming that $\wp$ is compactly supported and by a possible rescaling, we can restrict our attention to the Preisach unit triangle $\{(\beta,\alpha) \mid -1 \le \beta \le \alpha \le 1\}$ within the Preisach plane (see Fig. 6), which shows the Preisach unit triangle with the sets S^+, S^- of up- and down-switched relays at the initial state according to Equation (2).

We would now like to start with pointing out three characteristic features of hysteresis operators in general, and especially of Preisach operators (see Equation (1)), that will play a role in the following:

Firstly, the output $p(t)$ at some time t depends on the present as well as past states of the input $e(t)$, but not on the future (Volterra property).

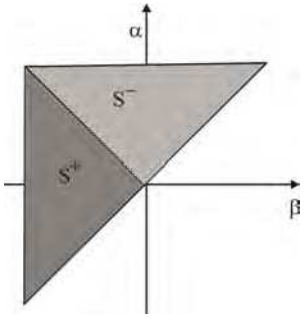

Fig. 6. Preisach plane at the initial state according to Equation (2).

Secondly, it is rate independent, i.e., the values that the output attains are independent of the speed of the input in the sense that for any continuous monotonically increasing transformation κ of the time interval $[0, T]$ with $\kappa(0) = 0$, $\kappa(T) = T$, and all input functions e, there holds

$$\mathcal{H}[e \circ \kappa] = \mathcal{H}[e] \circ \kappa \,. \tag{3}$$

As a consequence, given a piecewise monotone continuous input e, the output is (up to the speed in which it is traversed) uniquely determined by the local extrema of the input only, i.e.,the values of e at instances where e changes its monotonicity behavior from decreasing to increasing or vice versa.
The third important characteristic of hysteresis is that it typically does not keep the whole input history in mind but forgets certain passages in the past. I.e., there is a certain deletion in memory and it is quite important to take this into account also when doing computations: in a finite element simulation of a system with hysteresis, each element has its own history, so in order to keep memory consumption in an admissible range it is essential to delete past values that are not required any more.
Deletion, i.e., the way in which hysteresis operators forget, can be described by appropriate orderings on the set S of strings containing local extrema of the input, together with the above mentioned correspondence to piecewise monotone input functions.

Definition 1. *(Definition 2.7.1 in Brokate & Sprekels (1996))*
Let $\preceq$ be an ordering (i.e., a reflexive, antisymmetric, and transitive relation) on S. We say that a hysteresis operator forgets according to $\preceq$, if

$$s' \preceq s \;\Rightarrow \mathcal{H}(s) = \mathcal{H}(s') \quad \forall s, s' \in S$$

Due to this implication, strings can be reduced according to certain rules. With the notation

$$[[e, e']] := [\min\{e, e'\}, \max\{e, e'\}]$$

the relevant deletion rules for Preisach operators with neutral initial state Equation (2) can be written as follows (for an illustration see Fig. 7):

- *Monotone deletion rule:* only the local maxima and minima of the input are relevant.

$$\begin{aligned} &(e_0, \ldots, e_N) \mapsto (e_0, \ldots, e_{i-1}, e_{i+1}, \ldots, e_N) \\ &\text{if } e_i \in [[e_{i-1}, e_{i+1}]] \end{aligned} \tag{4}$$

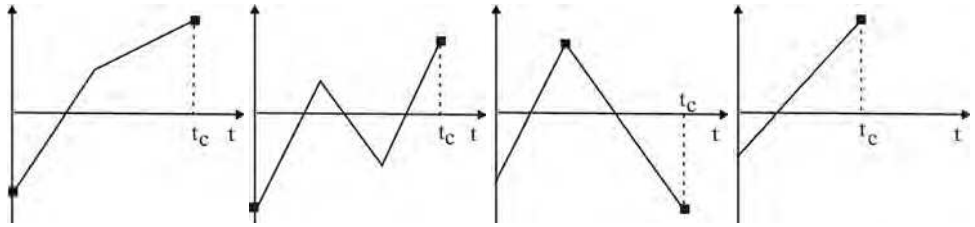

Fig. 7. Illustration of deletion rules according to Equation (4) - Equation (7). Here the filled boxes mark the dominant input values, i.e., those sufficing to compute output values after time t_c.

- *Madelung rule:* Inner minor loops are forgotten.

$$\begin{aligned}&(e_0,\ldots,e_N)\mapsto(e_0,\ldots,e_{i-1},e_{i+2},\ldots,e_N)\\&\text{if } [[e_i,e_{i+1}]]\subset[[e_{i-1},e_{i+2}]]\ \wedge\ e_i\notin[[e_{i-1},e_{i+1}]]\ \wedge\ e_{i+1}\notin[[e_i,e_{i+2}]]\end{aligned}\tag{5}$$

- *Wipe out:* previous absolutely smaller local maxima (minima) are erased from memory by subsequent absolutely larger local maxima (minima).

$$\begin{aligned}&(e_0,\ldots,e_N)\mapsto(e_1,\ldots,e_N)\\&\text{if } e_0\in[[e_1,e_2]]\end{aligned}\tag{6}$$

- *Initial deletion:* a maximum (minimum) is also forgotten if it is followed by an minimum (maximum) with sufficiently large modulus.

$$(e_0,\ldots,e_N)\mapsto(e_1,\ldots,e_N)\quad\text{if } |e_0|\le|e_1|\tag{7}$$

It can be shown that irreducible strings for this Preisach ordering with neutral initial state are given by the set

$$S_0=\{s\in S\mid s=(e_0,\ldots,e_N)\text{ is fading and }|e_0|>|e_1|\}$$

where

$$\begin{aligned}&s=(e_0,\ldots,e_N)\text{ is fading}\ \Leftrightarrow\\&\Big(s\in S_A\text{ and }|e_0-e_1|>|e_1-e_2|>|e_2-e_3|>\ldots>|e_{N-1}-e_N|\Big).\end{aligned}$$

Considering an arbitrary input string, the rules above have to be applied repeatedly to generate an irreducible string with the same output value, which could lead to a considerable computational effort. However, when computing the hysteretic evolution of some output function by a time stepping scheme, we update the input string and apply deletion in each time step and fortunately in that situation reduction can be done at low computational cost. Namely, only one iteration per time step is required and there is no need to recursively apply rules Equation (4)–Equation (7), see Lemma 3.3 in Kaltenbacher & Kaltenbacher (2006). After achieving an irreducible string $(e_0,\ldots,e_N)$, the hysteresis operator can be applied very

efficiently by just evaluation of a sum over the string entries

$$\mathcal{H}(s) = h(-e_0, e_0) + \sum_{k=1}^{N} h(e_{k-1}, e_k) \qquad \forall s = (e_0, \ldots, e_N) \tag{8}$$

instead of computing the integrals in Equation (1). In Equation (8) h is the so-called *shape function* or *Everett function* (cf. Everett (1955)), which can be precomputed according to

$$h(e_{N-1}, e_N) = 2\,\mathrm{sign}(e_N - e_{N-1}) \iint_{\Delta(e_{N-1}, e_N)} \wp(\beta, \alpha)\, d(\alpha, \beta)\,. \tag{9}$$

4. Piezoelectric model

We follow the basic ideas discussed in Kamlah & Böhle (2001) and decompose the physical quantities into a reversible and an irreversible part. For this purpose, we introduce the reversible part $\mathbf{D}^{\mathrm{r}}$ and the irreversible part $\mathbf{D}^{\mathrm{i}}$ of the dielectric displacement according to

$$\mathbf{D} = \mathbf{D}^{\mathrm{r}} + \mathbf{D}^{\mathrm{i}}\,. \tag{10}$$

In our case, using the general relation between dielectric displacement $\mathbf{D}$, electric field intensity $\mathbf{E}$, and polarization $\mathbf{P}$ we set $\mathbf{D}^{\mathrm{i}} = \mathbf{P}^{\mathrm{i}}$ (irreversible part of the electric polarization). Analogously to Equation (10), the mechanical strain $\mathbf{S}$ is also decomposed into a reversible part $\mathbf{S}^{\mathrm{r}}$ and an irreversible part $\mathbf{S}^{\mathrm{i}}$

$$\mathbf{S} = \mathbf{S}^{\mathrm{r}} + \mathbf{S}^{\mathrm{i}}\,. \tag{11}$$

The decomposition of the strain $\mathbf{S}$ is done in compliance with the theory of elastic-plastic solids under the assumption that the deformations are very small Bassiouny & Ghaleb (1989). That assumption is generally valid for piezoceramic materials with maximum strains below 0.2 %.

The reversible parts of mechanical strain $\mathbf{S}^{\mathrm{r}}$ and dielectric displacement $\mathbf{D}^{\mathrm{r}}$ are described by the linear piezoelectric constitutive law.

Now, in contrast to the thermodynamically motivated approaches in, e.g., Bassiouny & Ghaleb (1989); Kamlah & Böhle (2001); Landis (2004), we compute the polarization from the history of the driving electric field $\mathbf{E}$ by a scalar Preisach hysteresis operator $\mathcal{H}$

$$\mathbf{P}^{\mathrm{i}} = \mathcal{H}[\mathbf{E}]\ \mathbf{e}_P\,, \tag{12}$$

with the unit vector of the polarization $\mathbf{e}_P$, set equal to the direction of the applied electric field. Taking this into consideration, we currently restrict our model to uni-axially loaded actuators.

The butterfly curve for the mechanical strain could be modeled by an enhanced hysteresis operator as well. The use of an additional hysteresis operator for the strain can be avoided based on the following observation, though. As seen in Fig. 8, the mechanical strain S_{33} appears to be proportional to the squared dielectric polarization P_3, i.e., the relation $S^{\mathrm{i}} = \beta \cdot (\mathcal{H}[\mathbf{E}])^2$, with a model parameter β, seems obvious. To keep the model more general, we choose the ansatz

$$S^{\mathrm{i}} = \beta_1 \cdot \mathcal{H}[\mathbf{E}] + \beta_2 \cdot (\mathcal{H}[\mathbf{E}])^2 + \ldots + \beta_l \cdot (\mathcal{H}[\mathbf{E}])^l\,. \tag{13}$$

Similarly to Kamlah & Böhle (2001) we define the tensor of irreversible strains as follows

$$[\mathbf{S}^{\mathrm{i}}] = \tfrac{3}{2}\left(\beta_1 \cdot \mathcal{H}[\mathbf{E}] + \beta_2 \cdot (\mathcal{H}[\mathbf{E}])^2 + \cdots + \beta_l \cdot (\mathcal{H}[\mathbf{E}])^l\right)\left(\mathbf{e}_P\,\mathbf{e}_P{}^T - \tfrac{1}{3}\,[\mathbf{I}]\right). \tag{14}$$

The parameters $\beta_1 \ldots \beta_n$ need to be fitted to measured data.

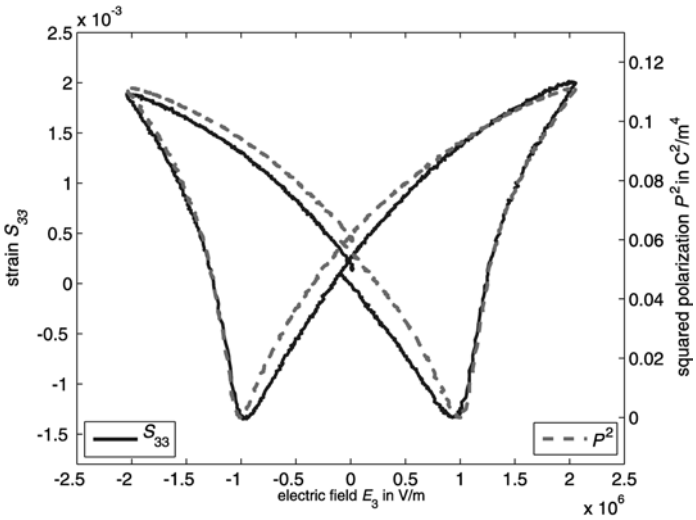

Fig. 8. Measured mechanical strain S_{33} and squared irreversible polarization P_3^{i} of a piezoceramic actuator on different axis.

Moreover, the entries of the tensor of piezoelectric moduli are now assumed to be a function of the irreversible electric polarization $\mathbf{P}^{\mathrm{i}}$. Here the underlying idea is that the piezoelectric properties of the material only appear once the material is poled. Without any polarization, the domains in the material are not aligned, and therefore coupling between the electric field and the mechanical field does not occur. If the polarization is increased, the coupling also increases. Hence, we define the following relation

$$[\mathbf{e}(\mathbf{P})] = \frac{|\mathbf{P}^{\mathrm{i}}|}{P_{\mathrm{sat}}^{\mathrm{i}}}\,[\mathbf{e}]\,. \tag{15}$$

Herein, $P_{\mathrm{sat}}^{\mathrm{i}}$ denotes the irreversible part of the saturation polarization $P_{\mathrm{sat}} = P_{\mathrm{sat}}^{\mathrm{r}} + P_{\mathrm{sat}}^{\mathrm{i}}$ (see state 2 in Fig. 3), $[\mathbf{e}]$ the tensor of constant piezoelectric moduli and $[\mathbf{e}(\mathbf{P}^{\mathrm{i}})]$ the tensor of variable piezoelectric moduli. Therewith, we model a uni-axial electric loading along a fixed polarization axis.
Finally, the constitutive relations for the electromechanical coupling can be established and written in e-form

$$\mathbf{S} = \mathbf{S}^{\mathrm{r}} + \mathbf{S}^{\mathrm{i}}\,;\;\; \mathbf{P}^{\mathrm{i}} = \mathcal{H}[\mathbf{E}]\mathbf{e}_P \tag{16}$$

$$\sigma = [\mathbf{c}^{\mathrm{E}}]\,\mathbf{S}^{\mathrm{r}} - [\mathbf{e}(\mathbf{P}^{\mathrm{i}})]^t\mathbf{E} \tag{17}$$

$$\mathbf{D} = [\mathbf{e}(\mathbf{P}^{\mathrm{i}})]\,\mathbf{S}^{\mathrm{r}} + [\varepsilon^{\mathrm{S}}]\,\mathbf{E} + \mathbf{P}^{\mathrm{i}} \tag{18}$$

or equivalently in d-form

$$\mathbf{S} = \mathbf{S}^{\mathrm{r}} + \mathbf{S}^{\mathrm{i}}\,;\;\; \mathbf{P}^{\mathrm{i}} = \mathcal{H}[\mathbf{E}]\mathbf{e}_P \tag{19}$$

$$\mathbf{S} = [\mathbf{s}^{\mathrm{E}}]\,\sigma + [\mathbf{d}(\mathbf{P}^{\mathrm{i}})]^t\mathbf{E} + \mathbf{S}^{\mathrm{i}} \tag{20}$$

$$\mathbf{D} = [\mathbf{d}(\mathbf{P}^{\mathrm{i}})]\,\sigma + [\varepsilon^{\sigma}]\,\mathbf{E} + \mathbf{P}^{\mathrm{i}}\,. \tag{21}$$

Due to the symmetry of the mechanical tensors, we use Voigt notation and write the mechanical stress tensor $[\sigma]$ as well as strain tensors $[\mathbf{S}]$ as six-component vectors (e.g., $\sigma = (\sigma_{xx}\,\sigma_{yy}\,\sigma_{zz}\,\sigma_{yz}\,\sigma_{xz}\,\sigma_{xy})^t = (\sigma_1\,\sigma_2\,\sigma_3\,\sigma_4\,\sigma_5\,\sigma_6)^t$). The relations between the different material tensors are as follows

$$[\mathbf{s}^{\mathrm{E}}] = [\mathbf{c}^{\mathrm{E}}]^{-1}\,;\;\; [\mathbf{d}]^t = [\mathbf{c}^{\mathrm{E}}]^{-1}[\mathbf{e}]^t\,;\;\; [\varepsilon^{\sigma}] = [\varepsilon^{\mathrm{S}}] + [\mathbf{d}]^t[\mathbf{e}]\,.$$

The governing equations for the mechanical and electrostatic fields are given by

$$\rho\ddot{\mathbf{u}} - \mathcal{B}^t\sigma - \mathbf{f} = 0\,;\;\; \boldsymbol{\nabla}\cdot\mathbf{D} = 0\,;\;\; \boldsymbol{\nabla}\times\mathbf{E} = 0\,, \tag{22}$$

see, e.g., Kaltenbacher (2007). In Equation (22) ρ denotes the mass density, $\mathbf{f}$ some prescribed mechanical volume force and $\ddot{\mathbf{u}} = \partial^2\mathbf{u}/\partial t^2$ the mechanical acceleration. Furthermore, the differential operator $\mathcal{B}$ is explicitely written as

$$\mathcal{B} = \begin{pmatrix} \frac{\partial}{\partial x} & 0 & 0 & 0 & \frac{\partial}{\partial z} & \frac{\partial}{\partial y} \\ 0 & \frac{\partial}{\partial y} & 0 & \frac{\partial}{\partial z} & 0 & \frac{\partial}{\partial x} \\ 0 & 0 & \frac{\partial}{\partial z} & \frac{\partial}{\partial y} & \frac{\partial}{\partial x} & 0 \end{pmatrix}^t . \tag{23}$$

With the same differential operator, we can express the mechanical strain - displacement relation

$$\mathbf{S} = \mathcal{B}\mathbf{u}\,. \tag{24}$$

Since the curl of the electric field intensity vanishes in the electrostatic case, we can fully describe this vector by the scalar electric potential φ, and write

$$\mathbf{E} = -\boldsymbol{\nabla}\varphi\,. \tag{25}$$

Combining the constitutive relations Equation (16) - (18) with the governing equations as given in Equation (22) together with Equation (24) and (25), we arrive at the following non-linear coupled system of PDEs

$$\rho\ddot{\mathbf{u}} - \mathcal{B}^T\left(\,[\mathbf{c}^E]\left(\mathcal{B}\mathbf{u} - \mathbf{S}^{\mathrm{i}}\right) + [\mathbf{e}(\mathbf{P}^{\mathrm{i}})]^t\boldsymbol{\nabla}\varphi\right) = 0 \tag{26}$$

$$\boldsymbol{\nabla}\cdot\left(\,[\mathbf{e}(\mathbf{P}^{\mathrm{i}})]\left(\mathcal{B}\mathbf{u} - \mathbf{S}^{\mathrm{i}}\right) - [\varepsilon^S]\boldsymbol{\nabla}\varphi + \mathbf{P}^{\mathrm{i}}\right) = 0 \tag{27}$$

with

$$\mathbf{P}^{\mathrm{i}} = \mathcal{H}[-\boldsymbol{\nabla}\varphi]\mathbf{e}_P \tag{28}$$

$$[\mathbf{S}^{\mathrm{i}}] = \left(\frac{3}{2}\sum_{i=0}^{l}\beta_i\left(\mathcal{H}[-\boldsymbol{\nabla}\varphi]\right)^i\right)\left(\mathbf{e}_P\,\mathbf{e}_P^T - \frac{1}{3}\mathbf{I}\right). \tag{29}$$

5. FE formulation

A straight forward procedure to solve Equation (26) and (27) is to put the hysteresis dependent terms (irreversible electric polarization and irreversible strain) to the right hand side and apply the FE method. Therewith, one arrives at a fixed-point method for the nonlinear system of equations. However, convergence can only be guaranteed if very small incremental steps are made within the nonlinear iteration process. A direct application of Newton's method is not possible, due to the lack of differentiability of the hysteresis operator. Therefore, we apply the so-called *incremental material parameter* method, which corresponds to a quasi Newton scheme applying a secant like linearization at each time step. For this purpose, we decompose the dielectric displacement $\mathbf{D}$ and the mechanical stress σ at time step t_{n+1} as follows

$$\mathbf{D}_{n+1} = \mathbf{D}_n + \Delta\mathbf{D}; \qquad \sigma_{n+1} = \sigma_n + \Delta\sigma\,. \tag{30}$$

Since we can assume, that $\mathbf{D}_n$ and σ_n have fulfilled their corresponding PDEs (the first two equations in Equation (22)) at time step t_n, we have to solve

$$\rho\Delta\ddot{\mathbf{u}} - \mathcal{B}^t\Delta\sigma - \Delta\mathbf{f} = 0 \qquad \boldsymbol{\nabla}\cdot\Delta\mathbf{D} = 0\,. \tag{31}$$

Now, we perform this decomposition also for our constitutive equations as given in Equation (20) and (21)

$$\mathbf{S}_n + \Delta\mathbf{S} = [\mathbf{s}^{\mathrm{E}}]\,(\sigma_n + \Delta\sigma) + \mathbf{S}^{\mathrm{i}}_n + \Delta\mathbf{S}^{\mathrm{i}} + \left([\mathbf{d}_n]^t + [\Delta\mathbf{d}]^t\right)(\mathbf{E}_n + \Delta\mathbf{E}) \tag{32}$$

$$\mathbf{D}_n + \Delta\mathbf{D} = \left([\mathbf{d}_n] + [\Delta\mathbf{d}]\right)(\sigma_n + \Delta\sigma) + [\boldsymbol{\varepsilon}^{\sigma}]\,(\mathbf{E}_n + \Delta\mathbf{E}) + \mathbf{P}^{\mathrm{i}}_n + \Delta\mathbf{P}^{\mathrm{i}}\,. \tag{33}$$

Again assuming equilibrium at time step t_n, we arrive at the equations for the increments

$$\Delta\mathbf{S} = [\mathbf{s}^{\mathrm{E}}]\,\Delta\sigma + [\mathbf{d}_{n+1}]^t\Delta\mathbf{E} + \Delta\mathbf{S}^{\mathrm{i}} + [\Delta\mathbf{d}]^t\mathbf{E}_n \tag{34}$$

$$\Delta\mathbf{D} = [\mathbf{d}_{n+1}]\Delta\sigma + [\boldsymbol{\varepsilon}^{\sigma}]\,\Delta\mathbf{E} + \Delta\mathbf{P}^{\mathrm{i}} + [\Delta\mathbf{d}]\sigma_n\,. \tag{35}$$

Now, we rewrite the two equations above as

$$\Delta\mathbf{S} = [\mathbf{s}^{\mathrm{E}}]\,\Delta\sigma + [\tilde{\mathbf{d}}_{n+1}]^t\Delta\mathbf{E} + [\Delta\mathbf{d}]^t\mathbf{E}_n \tag{36}$$

$$\Delta\mathbf{D} = [\mathbf{d}_{n+1}]\Delta\sigma + [\tilde{\boldsymbol{\varepsilon}}]\,\Delta\mathbf{E} + [\Delta\mathbf{d}]\sigma_n\,, \tag{37}$$

thus incorporating the hysteretic quantities in the material tensors. The coefficients of the newly introduced effective material tensors compute as follows

$$\tilde{\varepsilon}_{jj} = \varepsilon^{\sigma}_{jj} + \frac{\Delta P^{\mathrm{i}}_j}{\Delta E_j} \quad j = 1,2,3 \tag{38}$$

$$\left(\tilde{d}_{31}\right)_{n+1} = (d_{31})_{n+1} + \frac{\Delta S^{\mathrm{i}}_1}{\Delta E_z}\,; \quad \left(\tilde{d}_{32}\right)_{n+1} = (d_{32})_{n+1} + \frac{\Delta S^{\mathrm{i}}_2}{\Delta E_z} \tag{39}$$

$$\left(\tilde{d}_{33}\right)_{n+1} = (d_{33})_{n+1} + \frac{\Delta S^{\mathrm{i}}_3}{\Delta E_z}\,; \quad \left(\tilde{d}_{15}\right)_{n+1} = (d_{15})_{n+1}\,. \tag{40}$$

Since we need expressions for σ and $\mathbf{D}$ in order to solve Equation (31), we rewrite Equation (36) and (37) and obtain

$$\Delta\sigma = [\mathbf{c}^{\mathrm{E}}]\Delta\mathbf{S} - [\mathbf{c}^{\mathrm{E}}][\tilde{\mathbf{d}}_{n+1}]^t\Delta\mathbf{E} - [\mathbf{c}^{\mathrm{E}}][\Delta\mathbf{d}]^t\mathbf{E}_n \tag{41}$$

$$\Delta\mathbf{D} = [\mathbf{d}_{n+1}][\mathbf{c}^{\mathrm{E}}]\Delta\mathbf{S} + \left([\tilde{\varepsilon}] - [\mathbf{d}_{n+1}][\mathbf{c}^{\mathrm{E}}][\tilde{\mathbf{d}}_{n+1}]^t\right)\Delta\mathbf{E} - [\mathbf{d}_{n+1}][\mathbf{c}^{\mathrm{E}}][\Delta\mathbf{d}]^t\mathbf{E}_n + [\Delta\mathbf{d}]\sigma_n\,. \tag{42}$$

To simplify the notation, we make the following substitutions

$$[\mathbf{e}_{n+1}]^t = [\mathbf{c}^{\mathrm{E}}][\mathbf{d}_{n+1}]^t\,; \quad [\tilde{\mathbf{e}}_{n+1}]^t = [\mathbf{c}^{\mathrm{E}}][\tilde{\mathbf{d}}_{n+1}]^t$$
$$[\Delta\mathbf{e}]^t = [\mathbf{c}^{\mathrm{E}}][\Delta\mathbf{d}]^t\,; \quad [\tilde{\tilde{\varepsilon}}] = [\tilde{\varepsilon}] - [\mathbf{d}_{n+1}][\mathbf{c}^{\mathrm{E}}][\tilde{\mathbf{d}}_{n+1}]^t\,.$$

Substituting Equation (41) and (42) into Equation (31) results in

$$\rho\Delta\ddot{\mathbf{u}} - \mathcal{B}^t[\mathbf{c}^{\mathrm{E}}]\mathcal{B}\Delta\mathbf{u} - \mathcal{B}^t[\tilde{\mathbf{e}}_{n+1}]^t\tilde{\mathcal{B}}\Delta\varphi = \Delta\mathbf{f} + \mathcal{B}^t[\Delta\mathbf{e}]^t\boldsymbol{\nabla}\varphi_n \tag{43}$$

$$\boldsymbol{\nabla}\cdot[\mathbf{e}_{n+1}]\mathcal{B}\Delta\mathbf{u} - \boldsymbol{\nabla}\cdot[\tilde{\tilde{\varepsilon}}]\boldsymbol{\nabla}\Delta\varphi = -\boldsymbol{\nabla}\cdot[\mathbf{d}_{n+1}][\Delta\mathbf{e}]^t\boldsymbol{\nabla}\varphi_n - \boldsymbol{\nabla}\cdot[\Delta\mathbf{d}]\sigma_n\,. \tag{44}$$

This coupled system of PDEs with appropriate boundary conditions for $\mathbf{u}$ and φ defines the strong formulation for our problem. We now introduce the test functions $\mathbf{v}$ and ψ, multiply our coupled system of PDEs by these test functions and integrate over the whole computational domain Ω. Furthermore, by applying integration by parts[2], we arrive at the weak (variational) formulation: Find $\mathbf{u} \in (H_0^1)^3$ and $\varphi \in H_0^1$ such that[3]

$$\int_\Omega \rho\,\mathbf{v}\cdot\Delta\ddot{\mathbf{u}}\,\mathrm{d}\Omega + \int_\Omega(\mathcal{B}\mathbf{v})^t[\mathbf{c}^{\mathrm{E}}]\mathcal{B}\Delta\mathbf{u}\,\mathrm{d}\Omega + \int_\Omega(\mathcal{B}\mathbf{v})^t[\tilde{\mathbf{e}}_{n+1}]^t\boldsymbol{\nabla}\Delta\varphi\,\mathrm{d}\Omega \tag{45}$$
$$= \int_\Omega \mathbf{v}\cdot\Delta\mathbf{f}\,\mathrm{d}\Omega - \int_\Omega(\mathcal{B}\mathbf{v})^t[\Delta\mathbf{e}]\boldsymbol{\nabla}\varphi_n\,\mathrm{d}\Omega$$

$$\int_\Omega(\boldsymbol{\nabla}\psi)^t[\mathbf{e}_{n+1}]\mathcal{B}\Delta\mathbf{u}\,\mathrm{d}\Omega - \int_\Omega(\boldsymbol{\nabla}\psi)^t[\tilde{\tilde{\varepsilon}}]\boldsymbol{\nabla}\Delta\varphi\,\mathrm{d}\Omega \tag{46}$$
$$= -\int_\Omega(\boldsymbol{\nabla}\psi)^t[\mathbf{d}_{n+1}][\Delta\mathbf{e}]^t\boldsymbol{\nabla}\varphi_n\,\mathrm{d}\Omega$$
$$-\int_\Omega(\boldsymbol{\nabla}\psi)^t[\Delta\mathbf{d}]\sigma_n\,\mathrm{d}\Omega$$

for all test functions $\mathbf{v} \in (H_0^1)^3$ and $\psi \in H_0^1$. Now, using standard Lagrangian (nodal) finite elements for the mechanical displacement $\mathbf{u}$ and the electric scalar potential φ (n_{n} denotes the number of nodes with unknown displacement and unknown electric potential)

$$\Delta\mathbf{u} \approx \Delta\mathbf{u}^h = \sum_{i=1}^{d}\sum_{a=1}^{n_{\mathrm{n}}} N_a\Delta u_{ia}\mathbf{e}_i = \sum_{a=1}^{n_{\mathrm{n}}}\mathbf{N}_a\Delta\mathbf{u}_a\,; \quad \mathbf{N}_a = \begin{pmatrix} N_a & 0 & 0\\ 0 & N_a & 0\\ 0 & 0 & N_a\end{pmatrix} \tag{47}$$

[2] For simplicity we assume a zero mechanical stress condition on the boundary.
[3] H_0^1 is the space of functions, which are square integrable along with their first derivatives in a weak sense, Adams (1975).

$$\Delta\varphi \approx \Delta\varphi^h = \sum_{a=1}^{n_n} N_a \Delta\varphi_a \tag{48}$$

as well as for the test functions $\mathbf{v}$ and φ, we obtain the spatially discrete formulation

$$\begin{pmatrix} \mathbf{M}_{uu} & 0 \\ 0 & 0 \end{pmatrix} \begin{pmatrix} \Delta\underline{\ddot{\mathbf{u}}} \\ \Delta\underline{\ddot{\varphi}} \end{pmatrix} + \begin{pmatrix} \mathbf{K}_{uu} & \tilde{\mathbf{K}}_{u\varphi} \\ \mathbf{K}_{\varphi u} & -\tilde{\tilde{\mathbf{K}}}_{\varphi\varphi} \end{pmatrix} \begin{pmatrix} \Delta\underline{\mathbf{u}} \\ \Delta\underline{\varphi} \end{pmatrix} = \begin{pmatrix} \underline{f}_u \\ \underline{f}_\varphi \end{pmatrix} . \tag{49}$$

In Equation (49) the vectors $\Delta\underline{\mathbf{u}}$ and $\Delta\underline{\varphi}$ contain all the unknown mechanical displacements and electric scalar potentials at the finite element nodes. The FE matrices and right hand sides compute as follows

$$\mathbf{K}_{uu} = \bigwedge_{e=1}^{n_e} \mathbf{k}_{uu}^e \;;\; \mathbf{k}_{uu}^e = [\mathbf{k}_{pq}] \;;\; \mathbf{k}_{pq} = \int_{\Omega^e} \mathcal{B}_p^t [\mathbf{c}^E] \mathcal{B}_q \, \mathrm{d}\Omega \tag{50}$$

$$\tilde{\mathbf{K}}_{u\varphi} = \bigwedge_{e=1}^{n_e} \tilde{\mathbf{k}}_{u\varphi}^e \;;\; \tilde{\mathbf{k}}_{u\varphi}^e = [\tilde{\mathbf{k}}_{pq}] \;;\; \tilde{\mathbf{k}}_{pq} = \int_{\Omega^e} \mathcal{B}_p^t [\tilde{\mathbf{e}}_{n+1}]^t \hat{\mathcal{B}}_q \, \mathrm{d}\Omega \tag{51}$$

$$\mathbf{K}_{\varphi u} = \bigwedge_{e=1}^{n_e} \mathbf{k}_{\varphi u}^e \;;\; \mathbf{k}_{\varphi u}^e = [\mathbf{k}_{pq}] \;;\; \mathbf{k}_{pq} = \int_{\Omega^e} \hat{\mathcal{B}}_p^t [\mathbf{e}_{n+1}] \mathcal{B}_q \, \mathrm{d}\Omega \tag{52}$$

$$\tilde{\tilde{\mathbf{K}}}_{\varphi\varphi} = \bigwedge_{e=1}^{n_e} \tilde{\tilde{\mathbf{k}}}_{\varphi\varphi}^e \;;\; \tilde{\tilde{\mathbf{k}}}_{\varphi\varphi}^e = [\tilde{\tilde{\mathbf{k}}}_{pq}] \;;\; \tilde{\tilde{\mathbf{k}}}_{pq} = \int_{\Omega^e} \hat{\mathcal{B}}_p^t [\tilde{\tilde{\boldsymbol{\varepsilon}}}] \hat{\mathcal{B}}_q \, \mathrm{d}\Omega \tag{53}$$

$$\underline{f}_u = \bigwedge_{e=1}^{n_e} \underline{f}_u^e \;;\; \underline{f}_u^e = [\underline{f}_p] \tag{54}$$

$$\underline{f}_p = \int_{\Omega^e} \mathbf{N}_p \Delta\mathbf{f} \, \mathrm{d}\Omega - \int_{\Omega^e} \mathcal{B}_p^t [\Delta\mathbf{e}_{n+1}] \hat{\mathcal{B}} \psi_n \, \mathrm{d}\Omega$$

$$\underline{f}_\varphi = \bigwedge_{e=1}^{n_e} \underline{f}_\varphi^e \;;\; \underline{f}_\varphi^e = [\underline{f}_p] \tag{55}$$

$$\underline{f}_p = -\int_{\Omega^e} \mathcal{B}_p^t [\mathbf{d}_{n+1}] [\Delta\mathbf{e}]^t \hat{\mathcal{B}} \varphi_n \, \mathrm{d}\Omega - \int_{\Omega^e} \hat{\mathcal{B}}_p^t [\Delta\mathbf{d}] \sigma_n \, \mathrm{d}\Omega \, .$$

In Equation (50) - (55) n_e denotes the number of finite elements, $\bigwedge$ the FE assembly operator (assembly of element matrices to global system matrices) and $\mathcal{B}_p$, $\hat{\mathcal{B}}_p$ compute as

$$\mathcal{B}_p = \begin{pmatrix} \frac{\partial N_p}{\partial x} & 0 & 0 & 0 & \frac{\partial N_p}{\partial z} & \frac{\partial N_p}{\partial y} \\ 0 & \frac{\partial N_p}{\partial y} & 0 & \frac{\partial N_p}{\partial z} & 0 & \frac{\partial N_p}{\partial x} \\ 0 & 0 & \frac{\partial N_p}{\partial z} & \frac{\partial N_p}{\partial y} & \frac{\partial N_p}{\partial x} & 0 \end{pmatrix}^t$$

$$\hat{\mathcal{B}}_p = \left(\partial N_p/\partial x, \, \partial N_p/\partial y, \, \partial N_p/\partial z\right)^t .$$

Time discretization is performed by the Newmark scheme choosing respectively the values 0.25 and 0.5 for the two integration parameters β and γ to achieve 2nd order accuracy Hughes (1987). Therewith, we arrive at a predictor-corrector scheme that involves solution of a nonlinear system of algebraic equations of the form

$$\begin{pmatrix} \mathbf{K}^*_{uu} & \tilde{\mathbf{K}}_{u\varphi}(\Delta\underline{\mathbf{u}}, \Delta\underline{\varphi}) \\ \mathbf{K}_{\varphi u} & -\tilde{\tilde{\mathbf{K}}}^*_{\varphi\varphi}(\Delta\underline{\mathbf{u}}, \Delta\underline{\varphi}) \end{pmatrix} \begin{pmatrix} \Delta\underline{\mathbf{u}} \\ \Delta\underline{\varphi} \end{pmatrix} = \begin{pmatrix} \underline{g}_u(\Delta\underline{\mathbf{u}}, \Delta\underline{\varphi}) \\ \underline{g}_\varphi(\Delta\underline{\mathbf{u}}, \Delta\underline{\varphi}) \end{pmatrix}$$

with $\mathbf{K}^*_{uu}$, $\tilde{\tilde{\mathbf{K}}}^*_{\varphi\varphi}$ the effective stiffness matrices. The solution for each time step $(n+1)$ is obtained by solving this fully discrete nonlinear system of equations of the form $A(z)z = b(z)$ by the iteration $A(z_k)z_{k+1} = b(z_k)$ (often denoted as linearization by freezing the coefficients) until the following incremental stopping criterion is fulfilled

$$\frac{||\Delta\underline{\mathbf{u}}^{n+1}_{k+1} - \Delta\underline{\mathbf{u}}^{n+1}_{k}||_2}{||\Delta\underline{\mathbf{u}}^{n+1}_{k+1}||_2} + \frac{||\Delta\underline{\varphi}^{n+1}_{k+1} - \Delta\underline{\varphi}^{n+1}_{k}||_2}{||\Delta\underline{\varphi}^{n+1}_{k+1}||_2} < \delta_{\text{rel}} \tag{56}$$

with k the iteration counter. In our practical computations (see Sec. 7) we have set δ_{rel} to 10^{-4}. For further details we refer to Kaltenbacher et al. (2010).

6. Fitting of material parameters

The determination of all material parameters for our nonlinear piezoelectric model is a quite challenging task. Since we currently restrict ourselves to the uni-axial case, two experimental setups suffice to obtain the necessary measurement data for the fitting procedure.
According to our ansatz (decomposition into a reversible and an irreversible part of the dielectric displacement and mechanical strain) we have to determine the following parameters:

- entries of the constant material tensors $[\mathbf{s}^{\mathrm{E}}]$, $[\mathbf{d}]$, $[\varepsilon^{\sigma}]$ (see Equation (20) and Equation (21));
- weight function $\wp$ of the hysteresis operator (see Equation (1),
- polynomial coefficients $\beta_1, \ldots \beta_l$ for the irreversible strain (see Equation (13)).

The determination of the linear material parameters is performed by our enhanced inverse scheme, Kaltenbacher et al. (2006); Lahmer et al. (2008). To do so, we carry out electric impedance measurements on the actuator and fit the entries of the material tensors by full 3d simulations in combination with the inverse scheme. Figure 9 displays the experimental setup, where it can be seen that we electrically pre-load the piezoelectric actuator with a DC voltage. The amplitude of the DC voltage source is chosen in such a way that the piezoelectric material is driven into saturation. The reason for this pre-loading is the fact, that the irreversible physical quantities show saturation and a further increase beyond saturation is just given by the reversible physical quantities. These reversible quantities however, are modeled by the linear piezoelectric equations using the corresponding material tensors.
The data for fitting the hysteresis operator and for determination of the polynomial coefficients for the irreversible strain are collected by a second experimental setup as displayed in Fig. 10. A signal generator drives a power amplifier to generate the necessary input voltage. Thereby, we use a voltage driving sequence as shown in Fig. 10 to provide appropriate data for identifying the hysteretic behavior Mayergoyz (1991). The first peak

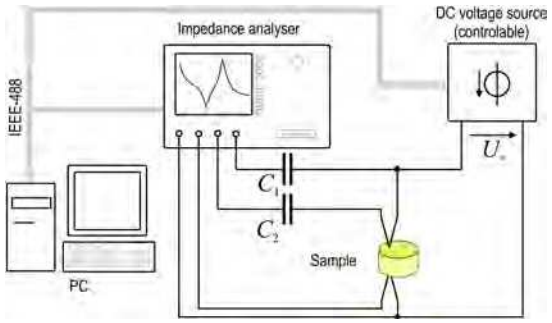

Fig. 9. Experimental setup for measuring the electric impedance at saturation of piezoelectric actuators.

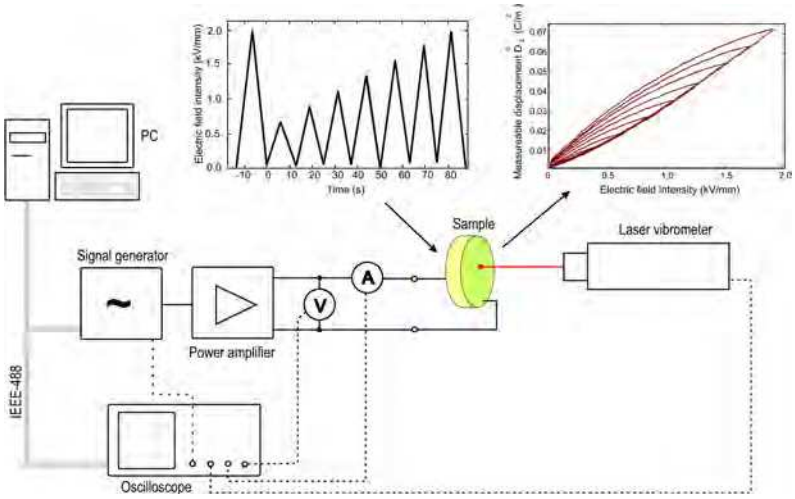

Fig. 10. Principle experimental setup for measuring the hysteresis curves of piezoelectric actuators.

within the excitation signal guarantees the same initial polarization for every measurement. The electric current $i(t)$ to the actuator is measured by an ampere-meter, the electric voltage $u(t)$ at the actuator by a voltmeter and the mechanical displacement $x(t)$ by a laser vibrometer. Now in the first step, we can compute the total electric displacement D_3 by

$$D_3(t) = P_{\text{rem}}^{\text{i}} + \frac{1}{A}\int_0^t i(\tau)\,\mathrm{d}\tau = P_{\text{rem}}^{\text{i}} + D_3^{\text{m}}(t)\,. \tag{57}$$

In Equation (57) A denotes the surface of the electrode, D_3^{m} the measurable electric displacement and $P_{\text{rem}}^{\text{i}}$ accounts for the fact, that for unipolar excitations the dielectric displacement does not return to zero for zero electric field (instead it returns to the remanent polarization, which cannot be determined by the current measurement but has to be measured separately). Furthermore, we compute the electric field intensity E_3 just by dividing the

applied electric voltage u by the distance between the actuator's electrodes. With the linear material parameters d_{33} and $\varepsilon_{33}^{\sigma}$ we can now compute a first guess for the irreversible polarization

$$P_{3,\mathrm{init}}^{\mathrm{i}}(t) = D_3(t) - d_{33}\sigma_3(t) - \varepsilon_{33}^{\sigma}E_3(t)\,. \tag{58}$$

Here σ_3 accounts for any mechanical preloading as in the case of the stack actuator or is set to zero as in the case of the disc actuator (stress-free boundary conditions). In the case of a clamped actuator, one will need an additional force sensor to determine σ_3.
By simply iterating between the following two equations

$$d_{33}(P_3) = \frac{P_3^{\mathrm{i}}}{P_{\mathrm{sat}}^{\mathrm{i}}}\, d_{33} \tag{59}$$

$$P_3^{\mathrm{i}} = D_3 - d_{33}(P_3^{\mathrm{i}})\sigma_3 - \varepsilon_{33}^{\sigma}E_3 \tag{60}$$

for each time instance t, we achieve at $P_3^{\mathrm{i}}(t)$ and $d_{33}(P_3^{\mathrm{i}}(t))$. Using Equation (20) we obtain the irreversible strain

$$S_3^{\mathrm{i}}(t) = S_3(t) - s_{33}^{\mathrm{E}}\sigma_3(t) - d_{33}(P_3^{\mathrm{i}}(t))E_3(t)\,, \tag{61}$$

where $S_3(t)$ has been computed from the measured displacement x and the geometric dimension of the actuator. Since S_3^{i} is now a known quantity, we solve a least squares problem to obtain the coefficients β_i according to our relation for the irreversible strain (see Equation (13))

$$\min_{(\beta_1\dots\beta_l)} \sum_{i=1}^{n_T} \left(\sum_{j=1}^{l} \beta_j \left(P_3^{\mathrm{i}}(t_i) \right)^j - S_3(t_i) \right)^2 \tag{62}$$

collocated to n_T discrete time instances t_i. Once the input $E_3(t)$ and the output $P_3(t)$ of the Preisach operator $\mathcal{H}$ are directly available, the problem of identifying the weight function $\wp$ amounts to a linear integral equation of the first kind

$$\iint_S \wp(\alpha,\beta)\mathcal{R}_{\beta,\alpha}[E_3](t)\, d\alpha\, d\beta = P_3(t) \qquad t \in \left[0, \bar{t}\right]. \tag{63}$$

Using a discretization of the Preisach operator as a linear combination of elementary hysteresis operators $\mathcal{H}_\lambda$

$$\mathcal{H} = \sum_{\lambda\in\Lambda} a_\lambda \mathcal{H}_\lambda \tag{64}$$

and evaluating the output at n_T discrete time instances $0 \le t_1 < t_2 < \cdots < t_{n_T} \le \bar{t}$, we approximate the solution of Equation (63) by solving a linear least squares problem for the coefficients $\mathbf{a} = (a_\lambda)_{\lambda\in\Lambda}$

$$\min_{\mathbf{a}} \sum_{i=1}^{n_T} \left(\sum_{\lambda\in\Lambda} a_\lambda \mathcal{H}_\lambda[E_3](t_i) - P_3(t_i) \right)^2. \tag{65}$$

In Equation (64), $\mathcal{H}_\lambda$ may be chosen as simple relays,

$$\mathcal{H}_\lambda = \mathcal{R}_{\beta_j,\alpha_i}\,,$$

see Section 3. The solution of Equation (65) provides the coefficients a_λ (see Fig. 11), which corresponds to a piecewise constant approximation of the weight function. In that case,

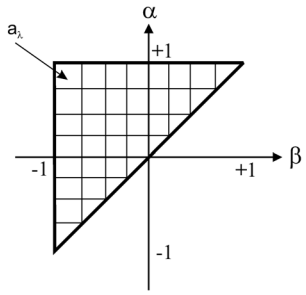

Fig. 11. Discretization of the Preisach plane by piecewise constants a_λ within each element.

obviously the set Λ consists of index pairs $\lambda = (i, j)$ corresponding to different up- and down-switching thresholds α_i, β_j and the array λ is supposed to be reordered in a column vector to yield a reformulation of Equation (65) in standard matrix form.
For further details of the fitting procedure, we refer to Hegewald (2008); Hegewald et al. (2008); Kaltenbacher & Kaltenbacher (2006); Rupitsch & Lerch. (2009).

7. Application

7.1 Piezoelectric disc actuator

In our first example we consider a simple disc actuator made of SP53 (CeramTec material) with a diameter of 35 mm and a thickness of 0.5 mm (see Fig. 12(a)).

(a) (b)

Fig. 12. Geometric setup and axisymmetric geometry used for FE simulation: (a) Geometric setup of the disc actuator; (b) FE model exploiting rotational symmetry as well as axial symmetry (for display reasons not true to scale).

We exploit both rotational and axial symmetry and end up with a two-dimensional axi-symmetric FE model (see Fig. 12(b)). Along the z-axis we set the radial and along the r-axis the axial displacement to zero. Furthermore, we set the electric potential to zero along the r-axis and apply half the measured electric voltage along the top electrode (since we model the disc actuator just by its half thickness).
First we perform an impedance measurement of the piezoelectric disc with an electric preloading (see Fig. 9) and apply our inverse scheme to obtain the entries of the material tensors, Lahmer et al. (2008). Second, we do measurements according the experimental setup in Fig. 10 and apply the fitting procedure as described in Sec. 6. The results for the constant

s_{11} (m^2/N)	s_{33} (m^2/N)	s_{12} (m^2/N)	s_{13} (m^2/N)	s_{66} (m^2/N)
$1,82 \cdot 10^{-11}$	$2,04 \cdot 10^{-11}$	$-4,85 \cdot 10^{-12}$	$-5,71 \cdot 10^{-12}$	$6,33 \cdot 10^{-11}$

d_{31} (C/N)	d_{33} (C/N)	d_{15} (C/N)	ε_{11} (F/m)	ε_{33} (F/m)
$-1,74 \cdot 10^{-10}$	$4,30 \cdot 10^{-10}$	$4,87 \cdot 10^{-10}$	$7,39 \cdot 10^{-9}$	$1,68 \cdot 10^{-8}$

(a)

ν	β_ν / $(m^2 \cdot C^{-1})^\nu$
1	$1{,}13 \cdot 10^{-2}$
2	$2{,}33 \cdot 10^{-1}$
3	$8{,}70 \cdot 10^{0}$
4	$7{,}06 \cdot 10^{1}$

(b)

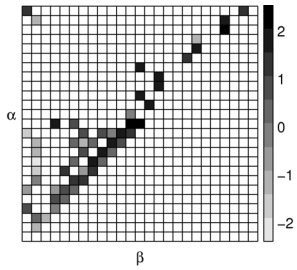

Table 1. Model parameters for the single disc actuator: (a) Material parameters and polynomial coefficients for the irreversible mechanical strain; (b) Logarithmic values of the Preisach weight function for $M = 25$.

material parameters, the polynomial coefficients for approximating the irreversible strain and the Preisach weight function are listed in Tab. 1.[4]

A FE simulation is performed with these fitted data, using the above described boundary conditions and a triangular excitation voltage different from the one used for the fitting procedure. The average number of nonlinear iterations within each time step to achieve the stopping criterion of (56) with an accuracy of $\delta_{\text{rel}} = 10^{-4}$ was only about two and no restriction on the time step size had to be imposed.

Figure 13 displays in detail the comparison of the measured and FE simulated data. This example clearly demonstrates, that using the fitted model parameters our FE scheme reproduces quite accurately the measured data in the experiment.

7.2 Piezoelectric revolving drive

The second practical example concerns a piezoelectric revolving motor as displayed in Fig. 14 Kappel et al. (2006). This drive operates in a large frequency range, and its main advantage is the compact construction and the high moment of torque. The rotary motion of the drive displayed in Fig. 14 results due to a sine-excitation of the two stack actuators with a 90 degree phase shift. The construction of the drive guarantees that shaft and clutch driving ring have a permanently contact at each revolving position.

[4] M, the discretization parameter for the Preisach plane, defines the number of discrete Preisach weights as $M(M+1)/2$.

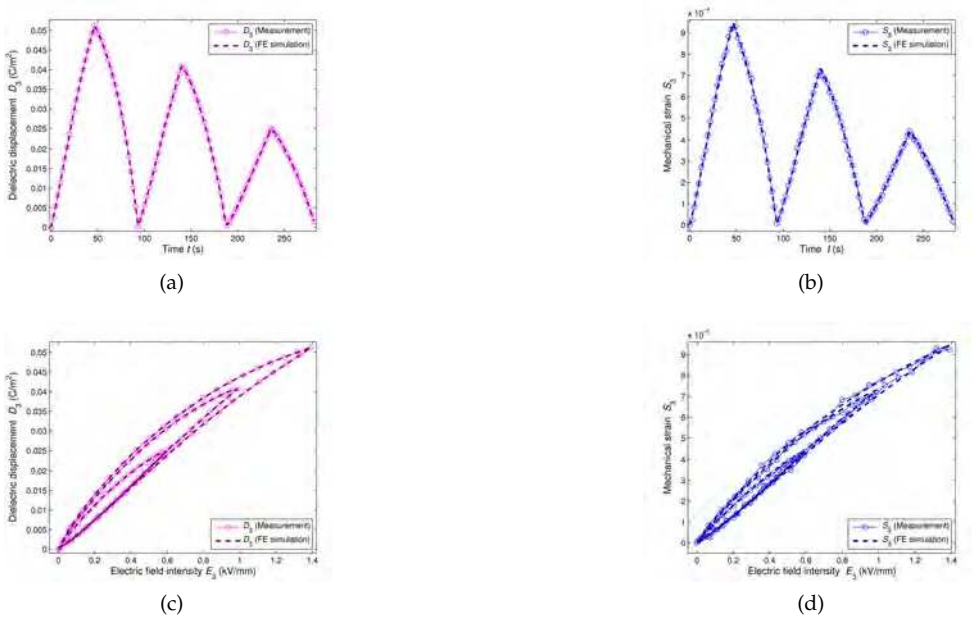

Fig. 13. Comparison of the measured and FE simulated data for the piezoelectric disc actuator: (a) Dielectric displacement over time; (b) Mechanical strain over time; (c) Dielectric displacement over electric field intensity; (d) Mechanical strain over electric field intensity.

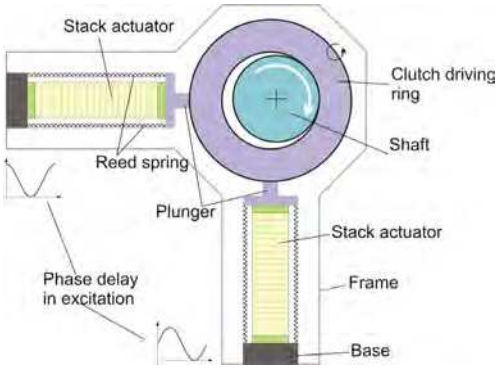

Fig. 14. Princple setup of the piezoelectric revolving drive Kappel et al. (2006)

The two stack actuators are of the same type, and their principle setup is displayed in Fig. 15(a). These stacks consists of 360 layers, each having a thickness of 80 μm and cross section of $6.8 \times 6.8\,\mathrm{mm}^2$. The overall length of the stack actuator is 30 mm and it exhibits a maximal stroke of 40 μm.

For the FE simulation we choose the full 3d setup and model the whole stack as one homogenized block. Since we currently restrict ourselves to the uni-axial electric load case, it makes no sense to fully resolve the inter-digital structure of the electrodes. Furthermore, we

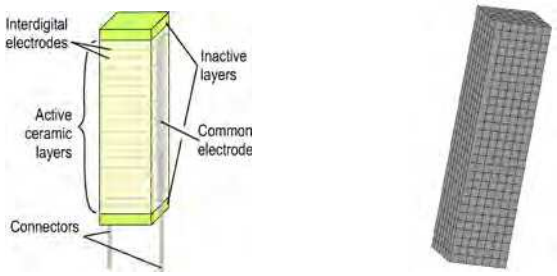

(a) (b)

Fig. 15. Geometric setup and FE model of stack actuator: (a) Geometric setup of the stack actuator; (b) Computational grid.

set the electric potential at the top surface to the measured voltage multiplied by the number of layers, since we do not resolve the layered structure.
Again, we do an impedance measurement at the electrically preloaded stack actuator and use our inverse scheme to get all entries of the material tensors. Next we use our measurement setup according to Fig. 10 and excite the stack actuator with a triangular signal. The material tensor entries as well as the polynomial coefficients for the irreversible strain and the Preisach weight function for the hysteresis operator are provided in Tab. 2.
Now in a second step, we use the fitted material parameters for our advanced piezoelectric material model and set up a FE model for the piezoelectric revolving drive as displayed in Fig. 16(a). For the clutch driving ring and plunger we apply standard material parameters of steel,

(a) (b)

Fig. 16. Piezoelectric revolving drive: (a) FE grid; (b) Strongly scaled (factor of about 150) mechanical deformation for a characteristic time step, when the left actuator is at maximal load.

and we do not model the shaft and its contact to the clutch driving ring. For the excitation we apply DC-shifted cosine- and sine-signals. The DC-shift guarantees, that the stack actuators are in an unipolar operating mode. The maximal achieved electric field intensity is about 2 kV/mm. In addition to the simulation, an experimental lab setup has been designed, where

s_{11} (m^2/N)	s_{33} (m^2/N)	s_{12} (m^2/N)	s_{13} (m^2/N)	s_{66} (m^2/N)
$1,29 \cdot 10^{-11}$	$2,54 \cdot 10^{-11}$	$-3.72 \cdot 10^{-12}$	$-5,85 \cdot 10^{-12}$	$3,39 \cdot 10^{-11}$

d_{31} (C/N)	d_{33} (C/N)	d_{15} (C/N)	ε_{11} (F/m)	ε_{33} (F/m)
$-8,09 \cdot 10^{-11}$	$2,83 \cdot 10^{-10}$	$2,52 \cdot 10^{-10}$	$5,82 \cdot 10^{-9}$	$0,81 \cdot 10^{-8}$

(a)

ν	β_ν / $(m^2 \cdot C^{-1})^\nu$
1	$1,79 \cdot 10^{-2}$
2	$6,60 \cdot 10^{-2}$
3	$8,13 \cdot 10^{-1}$
4	$1,91 \cdot 10^{1}$

(b)

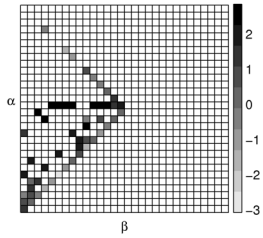

Table 2. Model parameters for the stack actuator: (a) Material parameters and polynomial coefficients for the irreversible mechanical strain; (b) Logarithmic values of the Preisach weight function for $M = 30$.

the shaft has also been neglected, Hegewald (2008). The displacements in x- and y-direction have been measured with a laser vibrometer.
In Fig. 16(b) we show the mechanical deformation of the whole considered setup for a characteristic time step, when the left stack actuator is at maximal stroke. A comparison between measured and simulated displacements both in x- and y-direction is displayed in Fig. 17. The fit for the displacement in x-direction is almost perfect; in y-direction there is some small difference.
Furthermore, in Fig. 18 we show the trajectory of one point on the ring. One observes that the resulting trajectory differs from a perfect circle. We also performed a simulation with a linear piezoelectric material model and obtained a perfect circle for the trajectory. Hence, the deviation from a perfect circle is clearly a result of the nonlinear (hysteretic) behavior of the stack actuators.

8. Summary and outlook

We have discussed a nonlinear piezoelectric model based on Preisach hysteresis operators and explained in detail the efficient solution of the governing partial differential equations by a quasi Newton scheme within the FE method. Moreover, we have described a procedure for determining the model parameters from measurements. Practical applications have

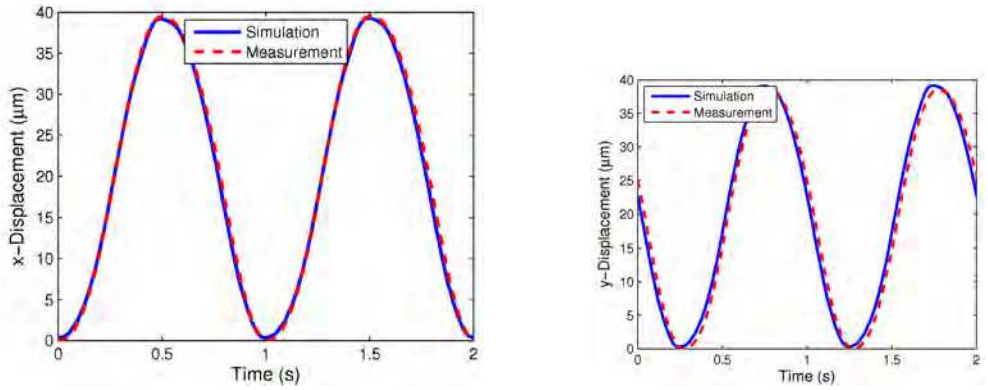

(a) (b)

Fig. 17. Comparison between measurement and simulation: (a) displacement in x-direction; (b) displacement in y-direction.

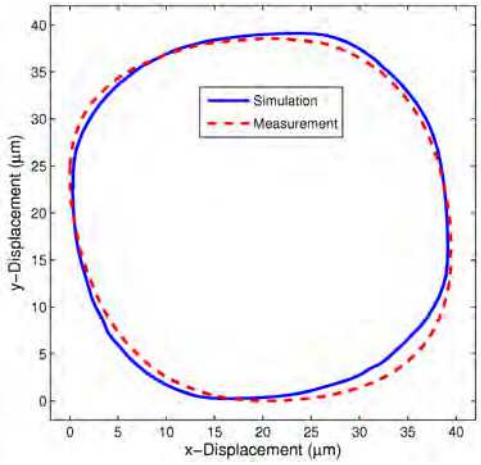

Fig. 18. Trajectory of one point of the ring obtained from measurements and simulation.

demonstrated, that the model is very well capable to provide qualitatively and quantitatively correct simulations.

Currently, we are investigating the extension of our model to also take ferroelastic loading into account. Such an approach can, e.g., be found in Ball et al. (2007). A very interesting option for modelling both ferroelectricity and ferroelasticity in a thermodynamically consistent manner is enabled by so-called hysteresis potentials, see Krejčí (2010).

Referring to Equation (28), Equation (29), we finally describe a possible extension to a multi-axial piezoelectric model. First of all, we have to apply a vector Preisach hysteresis model (see, e.g Mayergoyz (1991)), which for each electric field intensity vector **E** provides a

vector for the irreversible polarization $\mathbf{P}^{\mathrm{i}}$

$$\mathbf{P}^{\mathrm{i}} = \boldsymbol{\mathcal{H}}(\mathbf{E})\,. \tag{66}$$

Furthermore, we compute the coupling tensor $[\mathbf{e}(\mathbf{P}^{\mathrm{i}})]$ as in Equation (15) and rotate it in the direction of the irreversible polarization $\mathbf{P}^{\mathrm{i}}$. Similarly as in the scalar case, we define the irreversible strains by

$$[\mathbf{S}^{\mathrm{i}}] = \tfrac{3}{2}\left(\beta_1 \cdot |\boldsymbol{\mathcal{H}}[\mathbf{E}]| + \beta_2 \cdot |\boldsymbol{\mathcal{H}}[\mathbf{E}]|^2 + \cdots + \beta_n \cdot |\boldsymbol{\mathcal{H}}[\mathbf{E}]|^n\right)\left(\mathbf{e}_P\,\mathbf{e}_P{}^T - \tfrac{1}{3}\,[\mathbf{I}]\right) \tag{67}$$

with the unit vector of the irreversible polarization defined by $\mathbf{e}_P = \mathbf{P}^{\mathrm{i}}/|\mathbf{P}^{\mathrm{i}}|$.

9. References

Adams, R. A. (1975). *Sobolev Spaces*, Pure and Applied Mathematics, Academic Press.

Ball, B. L., Smith, R. C., Kim, S. J. & Seelecke, S. (2007). A stress-dependent hysteresis model for ferroelectric materials, *Journal of Intelligent Material Systems and Structures* 18: 69–88.

Bassiouny, E. & Ghaleb, A. F. (1989). Thermodynamical formulation for coupled electromechanical hysteresis effects: Combined electromechanical loading, *International Journal of Engineering Science* 27(8): 989–1000.

Belov, A. Y. & Kreher, W. S. (2006). Simulation of microstructure evolution in polycrystalline ferroelectrics ferroelastics, *Acta Materialia* 54: 3463 3469.

Brokate, M. & Sprekels, J. (1996). *Hysteresis and Phase Transitions*, Springer, New York.

Cimaa, L., Laboure, E. & Muralt, P. (2002). Characterization and model of ferroelectrics based on experimental preisach density, *Review of Scientific Instruments* 73(10).

Delibas, B., Arockiarajan, A. & Seemann, W. (2005). A nonlinear model of piezoelectric polycrystalline ceramics under quasi-static electromechanical loading, *Journal of Materials Science: Materials in Electronics* 16: 507–515.

Everett, D. (1955). A general approach to hysteresis, *Trans. Faraday Soc.* 51: 1551–1557.

Fröhlich, A. (2001). *Mikromechanisches Modell zur Ermittlung effektiver Materialeigenschaften von piezoelektrischen Polykristallen*, Dissertation, Universität Karlsruhe (TH), Forschungszentrum Karlsruhe.

Hegewald, T. (2008). *Modellierung des nichtlinearen Verhaltens piezokeramischer Aktoren*, PhD thesis, Universität Erlangen-Nürnberg, URL: http://www.opus.ub.uni-erlangen.de/ opus/volltexte/2008/875/, URN: urn:nbn:de:bvb:29-opus-8758.

Hegewald, T., Kaltenbacher, B., Kaltenbacher, M. & Lerch, R. (2008). Efficient modeling of ferroelectric behavior for the analysis of piezoceramic actuators, *Journal of Intelligent Material Systems and Structures* 19(10): 1117–1129.

Huber, J. E. (2006). Micromechanical modelling of ferroelectrics, *Current Opinion in Solid State and Materials Science* 9: 100–106.

Huber, J. E. & Fleck, N. A. (2001). Multi-axial electrical switching of a ferroelectric: theory versus experiment, *Journal of the Mechanics and Physics of Solids* 49: 785 811.

Hughes, D. C. & Wen, J. T. (1995). Preisach modeling and compensation for smart material hysteresis, *Proceedings: Active Materials and Smart Structures*, Vol. 2427, pp. 50–64.

Hughes, T. J. R. (1987). *The Finite Element Method*, 1 edn, Prentice-Hall, New Jersey.

Kaltenbacher, B. & Kaltenbacher, M. (2006). Modelling and iterative identification of hysteresis via Preisach operators in PDEs, *in* J. Kraus & U. Langer (eds), *Lectures on*

Advanced Computational Methods in Mechanics, de Gruyter, chapter 1, pp. 1–45. ISBN 978-3-11-019556-9.

Kaltenbacher, B., Lahmer, T., Mohr, M. & Kaltenbacher, M. (2006). PDE based determination of piezoelectric material tensors, *European Journal of Applied Mathematics* 17: 383–416.

Kaltenbacher, M. (2007). *Numerical Simulation of Mechatronic Sensors and Actuators*, 2. edn, Springer, Berlin. ISBN: 978-3-540-71359-3.

Kaltenbacher, M., Kaltenbacher, B., Hegewald, T. & Lerch, R. (2010). Finite element formulation for ferroelectric hysteresis of piezoelectric materials, *Journal of Intelligent Material Systems and Structures* 21: 773–785.

Kamlah, M. (2001). Feroelectric and ferroelastic piezoceramics - modeling of electromechanical hysteresis phenomena, *Continuum Mech. Thermodyn.* 13: 219–268.

Kamlah, M. & Böhle, U. (2001). Finite element analysis of piezoceramic components taking into account ferroelectric hysteresis behavior, *International Journal of Solids and Structures* 38: 605–633.

Kappel, A., Gottlieb, B., Schwebel, T., Wallenhauer, C. & Liess, H. (2006). Pad - piezoelectric actuator drive, *Proceedings of the 10th International Conference on New Actuators, ACTUATOR 2006*, Bremen, Germany, pp. 457–460.

Krasnoselskii, M. & Pokrovskii, A. (1989). *Systems with Hysteresis*, Springer, Heidelberg.

Krejčí, P. (1996). *Hysteresis, Convexity, and Dissipation in Hyperbolic Equations*, Gakkotosho, Tokyo.

Krejčí, P. (2010). An energetic model for magnetostrictive butterfly hysteresis, *5th International Workshop on MULTI-RATE PROCESSES & HYSTERESIS in Mathematics, Physics, Engineering and Information Sciences*. Pécs, Hungary.

Kuhnen, K. (2001). *Inverse Steuerung piezoelektrischer Aktoren mit Hysterese-, Kriech- und Superpositionsoperatoren*, Dissertation, Universität des Saarlandes, Saarbrücken.

Lahmer, T., Kaltenbacher, M., Kaltenbacher, B. & Lerch, R. (2008). FEM-Based Determination of Real and Complex Elastic, Dielectric and Piezoelectric Moduli in Piezoceramic Materials, *IEEE Transactions on Ultrasonics, Ferroelectrics, and Frequency Control* 55(2): 465–475.

Landis, C. M. (2004). Non-linear constitutive modeling of ferroelectrics, *Current Opinion in Solid State and Materials Science* 8: 59–69.

Linnemann, K., Klinkel, S. & Wagner, W. (2009). A constitutive model for magnetostrictive and piezoelectric materials, *International Journal of Solids and Structures* 46: 1149 1166.

Mayergoyz, I. D. (1991). *Mathematical Models of Hysteresis*, Springer-Verlag New York.

McMeeking, R. M., Landis, C. M. & Jimeneza, M. A. (2007). A principle of virtual work for combined electrostatic and mechanical loading of materials, *International Journal of Non-Linear Mechanics* 42(6): 831–838.

Pasco, Y. & Berry, A. (2004). A hybrid analytical/numerical model of piezoelectric stack actuators using a macroscopic nonlinear theory of ferroelectricity and a preisach model of hysteresis, *Journal of Intelligent Material Systems and Structures* 15: 375–386.

Rupitsch, S. J. & Lerch., R. (2009). Inverse method to estimate material parameters for piezoceramic disc actuators, *Applied Physics A* 97(4): :735–740.

Schröder, J. & Keip, M.-A. (2010). Multiscale modeling of electro–mechanically coupled materials: homogenization procedure and computation of overall moduli, *Proceedings of the IUTAM conference on multiscale modeling of fatigue, damage and fracture in smart materials*, Springer, Heidelberg.

Schröder, J. & Romanowski, H. (2005). A thermodynamically consistent mesoscopic model for transversely isotropic ferroelectric ceramics in a coordinate-invariant setting, *Archive of Applied Mechanics* 74: 863–877.

Smith, R. C., Seelecke, S., Ounaies, Z. & Smith, J. (2003). A free energy model for hysteresis in ferroelectric materials, *Journal of Intelligent Material Systems and Structures* 14: 719–737.

Su, Y. & Landis, C. M. (2007). Continuum thermodynamics of ferroelectric domain evolution: Theory, fnite element implementation and application to domain wall pinning, *Journal of the Mechanics and Physics of Solids* 55: 280 305.

Visintin, A. (1994). *Differential Models of Hysteresis*, Springer, Berlin.

Wang, J., Kamlah, M. & Zhang, T.-Y. (2010). Phase field simulations of low dimensional ferroelectrics, *Acta Mechanica* . (to appear).

Xu, B.-X., Schrade, D., Müller, R., Gross, D., Granzow, T. & Rödel, J. (2010). Phase field simulation and experimental investigation of the electro-mechanical behavior of ferroelectrics, *Z. Angew. Math. Mech.* 90: 623–632.

Zäh, D., Kiefer, B., Rosato, D. & Miehe, C. (2010). A variational homogenization approach to electro-mechanical hystereses, talk at the 3rd GAMM Seminar on Multiscale Material Modeling, Bochum.

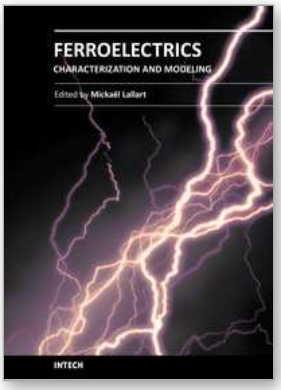

Ferroelectrics - Characterization and Modeling

Edited by Dr. MickaÃ«l Lallart

ISBN 978-953-307-455-9
Hard cover, 586 pages
Publisher InTech
Published online 23, August, 2011
Published in print edition August, 2011

Ferroelectric materials have been and still are widely used in many applications, that have moved from sonar towards breakthrough technologies such as memories or optical devices. This book is a part of a four volume collection (covering material aspects, physical effects, characterization and modeling, and applications) and focuses on the characterization of ferroelectric materials, including structural, electrical and multiphysic aspects, as well as innovative techniques for modeling and predicting the performance of these devices using phenomenological approaches and nonlinear methods. Hence, the aim of this book is to provide an up-to-date review of recent scientific findings and recent advances in the field of ferroelectric system characterization and modeling, allowing a deep understanding of ferroelectricity.

InTech Europe
University Campus STeP Ri
Slavka Krautzeka 83/A
51000 Rijeka, Croatia
Phone: +385 (51) 770 447
Fax: +385 (51) 686 166
www.intechopen.com

InTech China
Unit 405, Office Block, Hotel Equatorial Shanghai
No.65, Yan An Road (West), Shanghai, 200040, China
中国上海市延安西路65号上海国际贵都大饭店办公楼405单元
Phone: +86-21-62489820
Fax: +86-21-62489821